Chinese Chemical Letters 37 (2026) 111515

Contents lists available at ScienceDirect

Chinese Chemical Letters

journal homepage: www.elsevier.com/locate/cclet

# Enhanced luminescence efficiency and stability in Mn-based organic-inorganic hybrid metal halides *via* chlorination effect

Xiulian Cai[a,c,d], Qilin Wei[a,c,d], Yaping Gong[g], Tong Chang[a,c,d,*], Tongtong Kou[a,c,d], Ziyang Song[a,c,d], Zengshan Yue[a,c,d], Huanxin Su[a,c,d], Yuanxiang You[a,c,d], Chengmin Ji[e], Xinxin Han[f], Shiguo Han[a,b,c,d,*], William W. Yu[a,c,d,*]

[a] *School of Chemistry and Chemical Engineering, Shandong University, Ji'nan 250100, China*
[b] *Shenzhen Research Institute of Shandong University, Shenzhen 518000, China*
[c] *Key Laboratory of Special Functional Aggregated Materials, Ministry of Education, Shandong Key Laboratory of Advanced Organosilicon Materials and Technologies, Ji'nan 250100, China*
[d] *Shandong Provincial Key Laboratory for Science of Material Creation and Energy Conversion, Science Center for Material Creation and Energy Conversion, Qingdao 266237, China*
[e] *Fujian Science & Technology Innovation Laboratory for Optoelectronic Information of China, Fuzhou 350108, China*
[f] *School of Physical Science and Technology, Guangxi University, Nanning 530004, China*
[g] *Shandong Sport University, Ji'nan 250102, China*

ARTICLE INFO

*Article history:*
Received 28 April 2025
Revised 25 June 2025
Accepted 25 June 2025
Available online 26 June 2025

*Keywords:*
Manganese halide
Luminescence
Chlorination effect
Photophysical properties
Stability

ABSTRACT

Mn-based organic-inorganic hybrid metal halides have attracted extensive attention due to their excellent luminescence properties, easy processing, low cost, and non-toxicity. Herein, we effectively improved the luminescence properties and stability of the $[C_6H_{14}N]_2MnBr_4$ adopting the chlorination effect. Specifically, through the introduction of chlorine atom on the cations, the Mn-Mn distance in $[C_6H_{13}NCl]_2MnBr_4$ increases from 8.061 Å to 8.668 Å, thereby suppressing excitation energy transfer between adjacent $Mn^{2+}$ centers and enhancing the overall luminescent efficiency from 38.8 % to 74.5 %. Further experimental and theoretical analyses reveal that such chlorination effect increased the H···Cl interactions, significantly improving the environmental stability of Mn-based metal halides. Moreover, compare to $[C_6H_{14}N]_2MnBr_4$, the CIE chromaticity coordinates of $[C_6H_{13}NCl]_2MnBr_4$ are much closer to the NTSC green standard (0.23, 0.69). Our work provides new insights into the relationship between the cation structure and optical properties in Mn-based metal halides and sheds light on the design of stable metal halide materials.

© 2026 Published by Elsevier B.V. on behalf of Chinese Chemical Society and Institute of Materia Medica, Chinese Academy of Medical Sciences.

In recent years, organic-inorganic metal halides (OIMHs) have received intensive and continuous attention owing to their unique photoluminescence and electroluminescence properties in various fields such as solar cells, light-emitting diodes (LEDs), biological imaging, anti-counterfeiting labeling, scintillators, and sensors [1–10]. Among them, lead (Pb)-based metal halides have shown remarkable potentials in liquid crystal backlight displays and solid-state lighting due to their excellent optical properties (high photoluminescence quantum yield, narrow emission linewidth, tunable optical bandgap), outstanding defect tolerance and simple synthesis procedures [11,12]. Despite the great advances of Pb-based metal halides, they still suffers from two major problems, *i.e.*, the poor stability and the potential toxicity of the heavy metal Pb, which have become the biggest obstacles to their large-scale commercial applications [13,14]. Therefore, the development of new environmentally friendly, efficient, and stable metal halide materials with excellent luminescence property has become an imminent task [15–18].

Manganese (Mn)-based OIMHs offer not only the key advantages of Pb-based materials, such as high emission quantum efficiency, facile synthesis, and low cost, but also exhibit long-lived phosphorescence emission, friction luminescence, and low toxicity. These attributes make them ideal alternatives to Pb-based metal halide fluorescent materials [19–22]. In general, Mn-based OIMHs can achieve green and red emission by changing the crystal field strength. According to the crystal field theory, the coordination of $Mn^{2+}$ ions with organic molecules has a great influence on the optical properties. Due to the change of coordination environment, d-state leaps from $Mn^{2+}$ ions $^4T_1$–$^6A_1$ can relax with different emission colors [23–26]. The octahedrally coordinated Mn(II) with

* Corresponding authors.
*E-mail addresses:* chtoon@sdu.edu.cn (T. Chang), sghan@sdu.edu.cn (S. Han), wyu6000@gmail.com (W.W. Yu).

https://doi.org/10.1016/j.cclet.2025.111515
1001-8417/© 2026 Published by Elsevier B.V. on behalf of Chinese Chemical Society and Institute of Materia Medica, Chinese Academy of Medical Sciences.

higher field strengths exhibits low-energy red emission, while the tetrahedrally coordinated Mn(II) with lower field strengths exhibits high-energy green emission [27,28].

Human eyes are more sensitive to green and can even distinguish slight changes in hue [29]. Under this circumstance, it is crucial to design high-performance green emitters with the desired emission wavelength and bandwidth, high photoluminescence quantum yield (PLQY), and excellent thermal stability [30,31]. Generally, the OIMHs always display broad emission spectra due to the strong electron-phonon coupling in their soft and deformable lattices [32]. However, Mn-based OIMHs generally maintain relatively fixed emission characteristics. This is because the luminescence properties of $Mn^{2+}$ ions are primarily governed by their coordination environment and exhibit relatively low sensitivity to lattice distortion [33]. That is, modulating polyhedral distortion through strategic selection of organic ligands allows for precise control over emission peak positions in Mn-based OIMHs. Additionally, choosing different organic cations can control the inter-Mn tetrahedron distances, thereby suppressing excitation energy transfer between adjacent $Mn^{2+}$ centers and enhancing the overall luminescent efficiency. Therefore, by selecting different organic cations to fine-tune the structural distortion of Mn-coordinated tetrahedron and their distance, ideal green light emission can be achieved.

Inspired by the polyhedron regulation in OIMHs, we selected 1-methylpiperidine $C_6H_{13}N$ and 4–chloro-1-methylpiperidine $C_6H_{12}ClN$ as organic ligands to combine with $Mn^{2+}$ ions, synthesizing two 0D compounds, $[C_6H_{14}N]_2MnBr_4$ and $[C_6H_{13}NCl]_2MnBr_4$. Structural and luminescence analysis results indicate that both compounds contain isolated $[MnBr_4]^{2-}$ tetrahedron, leading to bright green emission. The structural transformation caused by changes in organic cations not only enables fine-tuning of the emission color but also increases the distance between $[MnBr_4]^{2-}$ tetrahedron, effectively suppressing excessive energy dissipation and yielding a nearly doubled PLQY (from 38.8 % to 74.5 %). Further experimental and theoretical analyses reveal that, compared to $[C_6H_{14}N]^+$, the introduction of $[C_6H_{13}NCl]^+$ increased the H···Cl interactions, significantly improving the environmental stability of $[C_6H_{13}NCl]_2MnBr_4$. Under ambient conditions (30 %–60 % RH and 10–23 °C), the crystallinity of $[C_6H_{13}NCl]_2MnBr_4$ remains unchanged after being placed for 4 months. Moreover, $[C_6H_{13}NCl]_2MnBr_4$ exhibits an emission color closer to the standard green light compared to $[C_6H_{14}N]_2MnBr_4$. Our work provides insights into the polyhedral regulation of luminescence properties in OIMHs and offers guidance for the design and optimization of novel, efficient, and stable metal halide luminescent materials.

Two single-crystal compounds were obtained through a cooling crystallization method by selecting $C_6H_{13}N$ and $C_6H_{12}ClN$ cations, respectively. The bulk crystals of $[C_6H_{14}N]_2MnBr_4$ and $[C_6H_{13}NCl]_2MnBr_4$ appear green and transparent under natural light. Both of them exhibit bright green light emission under 365 nm excitation (Fig. S1 in Supporting information). Single-crystal data analysis (Table S1 in Supporting information) revealed that $[C_6H_{14}N]_2MnBr_4$ belongs to the monoclinic crystal system with a centrosymmetric space group of $P2_1/c$ (Fig. 1, left), while $[C_6H_{13}NCl]_2MnBr_4$ belongs to the orthorhombic crystal system with a polar space group of $Pna2_1$ (Fig. 1, right). The PXRD patterns of $[C_6H_{14}N]_2MnBr_4$ and $[C_6H_{13}NCl]_2MnBr_4$ match well with their simulated XRD patterns, confirming the high purity of these synthesized compounds (Fig. S2 in Supporting information). Detailed analysis of the single-crystal structures indicates that both compounds exhibit a typical 0D crystal structure. In this structure, four $Br^-$ ions coordinate with one $Mn^{2+}$ ion to form an isolated $[MnBr_4]^{2-}$ tetrahedral unit. The cations ($[C_6H_{14}N]^+$ or $[C_6H_{13}NCl]^+$) not only separate the tetrahedral units within the structure but also serve to maintain charge balance. Due to the introduction of chlorine atoms, the Mn-Mn distance increases from 8.061 Å to 8.668 Å.

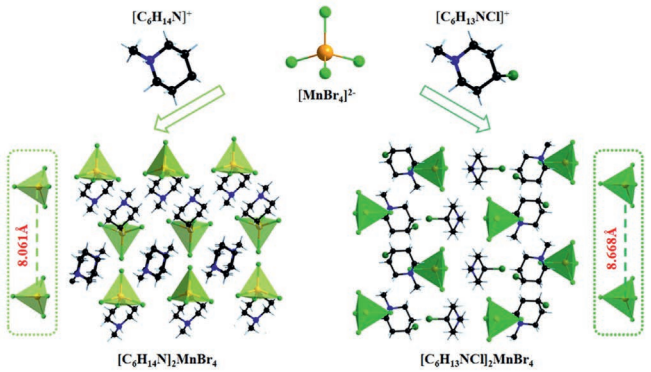



**Fig. 1.** Schematic demonstration of the crystal structures of $[C_6H_{14}N]_2MnBr_4$ (left) and $[C_6H_{13}NCl]_2MnBr_4$ (right).

In order to study the mechanism of luminescence, photoluminescent excitation (PLE), photoluminescent (PL) and ultraviolet-visible (UV–vis) absorption spectra were collected based on the two compounds. As a result, the PLE spectrum of $[C_6H_{14}N]_2MnBr_4$ reveals multiple absorption transitions at 277, 292, 363, 376, 437, 453, and 470 nm (Fig. 2a). These transitions correspond to the following $Mn^{2+}$ electronic transitions: $^6A_1(S) \rightarrow {}^4A_2(F)$, $^6A_1(S) \rightarrow {}^4T_1(F)$, $^6A_1(S) \rightarrow {}^4E(D)$, $^6A_1(S) \rightarrow {}^4A_1$, $^4E(G)$, $^6A_1(S) \rightarrow {}^4T_2(G)$, and $^6A_1(S) \rightarrow {}^4T_1(G)$, respectively [34]. The absorption spectrum of $[C_6H_{14}N]_2MnBr_4$ (Fig. 2b) also confirms the existence of these transition absorptions. The optical band gap of $[C_6H_{14}N]_2MnBr_4$ is calculated to be approximately 2.38 eV based on the Kubelka–Munk (K–M) function. Furthermore, under excitation at 363 nm, $[C_6H_{14}N]_2MnBr_4$ exhibits narrowband green emission at 533 nm with a full width at half maximum (FWHM) of 62 nm. The emission peak positions under different excitation wavelengths (Fig. S3a in Supporting information) remain nearly unchanged, confirming that $[C_6H_{14}N]_2MnBr_4$ has a consistent green emission source originating from a single luminescent center. Furthermore, the PL decay curves of $[C_6H_{14}N]_2MnBr_4$ (Fig. S4a in Supporting information, $\lambda_{ex} = 363$ nm, $\lambda_{em} = 533$ nm) exhibit a single exponential decay profile. The fitted millisecond-scale lifetime (0.27 ms) matches the characteristic radiative transition of $Mn^{2+}$ ions, directly proving that the 533 nm emission arises from $Mn^{2+}$ centers [35].

Although the PLE spectrum of $[C_6H_{13}NCl]_2MnBr_4$ is roughly the same as that of $[C_6H_{14}N]_2MnBr_4$, the PL emission characteristics of $[C_6H_{13}NCl]_2MnBr_4$ are significantly different from that of $[C_6H_{14}N]_2MnBr_4$, with the PL peak center wavelength shifted to 522 nm and the FWHM reduced to 48 nm (Fig. 2d). In addition, the light absorption range of $[C_6H_{13}NCl]_2MnBr_4$ is slightly broader than that of $[C_6H_{14}N]_2MnBr_4$ (Fig. 2e). Its optical band gap is calculated to be approximately 2.25 eV based on the K-M function [36]. The excitation dependent spectra and the fitting results of PL decay lifetime of $[C_6H_{13}NCl]_2MnBr_4$ also prove that the emission comes from $Mn^{2+}$ ion (Figs. S3b and S4b in Supporting information). The blue shift in peak position and the narrowing of the FWHM can be attributed to the chlorination effect, which causes $[C_6H_{13}NCl]^+$ to occupy a larger space compared to $[C_6H_{14}N]^+$, leading to an enhanced ordering in the $[C_6H_{13}NCl]_2MnBr_4$ crystal. This results in an increase in the Mn-Mn distance and enhanced ligand electronegativity, which intensifies the splitting of $Mn^{2+}$ ion energy levels, thereby increasing the excitation energy and causing the blue shift. At the same time, the interaction and energy dissipation between $Mn^{2+}$ ions are reduced, leading to a more concentrated emission and a narrower FWHM. Additionally, the reduction in the distor-

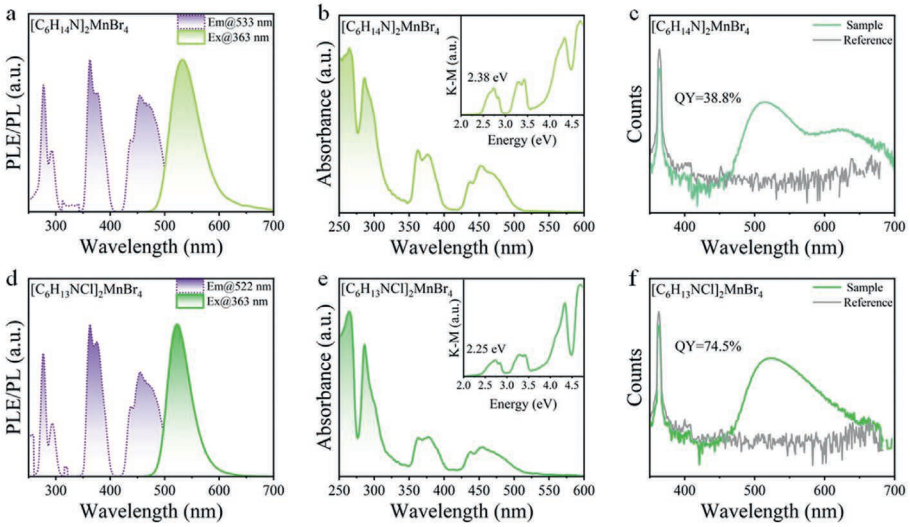



**Fig. 2.** (a) PLE and PL spectra of $[C_6H_{14}N]_2MnBr_4$. (b) UV–vis absorption spectrum and optical band gap of $[C_6H_{14}N]_2MnBr_4$. (c) PLQY of $[C_6H_{14}N]_2MnBr_4$. (d) PLE and PL spectra of $[C_6H_{13}NCl]_2MnBr_4$. (e) UV–vis absorption spectrum and optical band gap of $[C_6H_{13}NCl]_2MnBr_4$. (f) PLQY of $[C_6H_{13}NCl]_2MnBr_4$.

tion of the $[MnBr_4]^{2-}$ tetrahedron, which weakens the electron-phonon coupling, also contributes to the blue shift and narrowing of the FWHM (Fig. S5 in Supporting information).

In addition to the change in PL characteristics, the PLQY of $[C_6H_{13}NCl]_2MnBr_4$ nearly doubled compared to $[C_6H_{14}N]_2MnBr_4$, increasing from 38.8 % to 74.5 % (Figs. 2c and f). This significant change in PLQY can be attributed to the effect of different cations on crystal structure. Specifically, compared to $[C_6H_{14}N]^+$, the substitution of a hydrogen atom with a chlorine atom in $[C_6H_{13}NCl]^+$ causes a change in the electron cloud, making $[C_6H_{13}NCl]^+$ occupy a larger space. This change leads to an increase in the nearest Mn-Mn distance from 8.061 Å to 8.668 Å. The degree of overlap between electron clouds decreases, and the dipole-dipole interaction and the symmetry-guided spin-exchange interaction are weakened, resulting in a reduction in the energy transfer process between adjacent $Mn^{2+}$ centers [37]. This is equivalent to reducing concentration quenching without the need to use dopant activator ions, which is beneficial for achieving a higher PLQY. Additionally, a double-peak phenomenon appears in Fig. 2c. This is due to the significant distortion of the $[MnBr_4]^{2-}$ tetrahedron in $[C_6H_{14}N]_2MnBr_4$, which creates a complex local lattice environment and enhances electron-phonon coupling (manifested as a large $S$ value), promoting the stable formation of self-trapped excitons (STEs). These STEs recombine through different energy valleys or phonon-assisted channels, generating a secondary emission peak above 600 nm in addition to the intrinsic peak, resulting in a double peak. In $[C_6H_{13}NCl]_2MnBr_4$, the introduction of chloride atoms alters the interaction between the cations and $[MnBr_4]^{2-}$ anions, suppressing excessive tetrahedral distortion. This weakens the electron-phonon coupling (a small $S$ value), making it difficult to stabilize multi-channel recombination of STEs, and only the intrinsic single peak is observed.

To further explore the electron-phonon coupling of $[C_6H_{14}N]_2MnBr_4$ and $[C_6H_{13}NCl]_2MnBr_4$, we investigated their temperature-dependent PL in a range of 80–300 K (Figs. 3a and d). As the temperature increased, the PL intensities of both $[C_6H_{14}N]_2MnBr_4$ and $[C_6H_{13}NCl]_2MnBr_4$ gradually decreased. This phenomenon is due to the fact that the non-radiative recombination centers become active upon heating and capture more photogenerated carriers, thus reducing the probability of radiative transitions. Moreover, compared with $[C_6H_{13}NCl]_2MnBr_4$, the PL peak position of $[C_6H_{14}N]_2MnBr_4$ exhibited an obvious blue shift, and the FWHM of the emission band increased significantly with the increase in temperature. Generally speaking, in a 0D structure, the blue shift is mainly caused by the decrease in crystal field strength resulting from the thermal expansion of the host lattice [38]. The compound $[C_6H_{14}N]_2MnBr_4$ exhibits more pronounced thermal expansion due to differences in the cation structures and interactions. The $[C_6H_{14}N]^+$ cations primarily interact through weak van der Waals forces, resulting in a highly flexible structure. Upon heating, thermal motion easily breaks these weak interactions, causing a significant expansion of the lattice. In contrast, the $[C_6H_{13}NCl]^+$ cations experience stronger interactions, facilitated by the chloride atoms. These interactions enhance both the cation-cation and cation-anion bonds, thus restricting the lattice and minimizing thermal expansion. Consequently, $[C_6H_{14}N]_2MnBr_4$ shows significant thermal expansion, which leads to a blue shift in its luminescence. In addition, the increase in temperature also leads to more excited electrons diffusing to higher vibrational energy levels and then undergoing radiative transitions back to the ground state from these different energy levels, thereby widening the FWHM of the emission band.

Next, we analyzed two key values related to temperature. First, the Huang-Rhys factor $S$ is determined by fitting the below formula [39].

$$\mathrm{FWHM}(T) = 2.36\sqrt{S}\hbar\omega_{\mathrm{phonon}}\sqrt{\coth\frac{\hbar\omega_{\mathrm{phonon}}}{2K_{\mathrm{B}}T}} \quad (1)$$

where FWHM($T$) is the full width at half maximum at the experimental temperature, $S$ is electron-phonon coupling, $\hbar\omega_{\mathrm{phonon}}$ is the phonon frequency, $K_{\mathrm{B}}$ is the Boltzmann constant, and $T$ is the experimental temperature. Based on the fitting of Eq. 1, the Huang-Rhys factors ($S$) for $[C_6H_{14}N]_2MnBr_4$ and $[C_6H_{13}NCl]_2MnBr_4$ are calculated to be 15.85 and 7.89, respectively (Figs. 3b and e). A comparison reveals that the chlorination effect leads to a significant reduction in the electron-phonon coupling in $[C_6H_{13}NCl]_2MnBr_4$. This is due to the fact that chlorination makes the $[MnBr_4]^{2-}$ tetrahedral structure more regular, reducing the localized phonon modes induced by lattice distortion, weakening the electron-phonon energy exchange, and consequently leading to a significant decrease in the $S$ value from the PL spectrum fitting. This confirms the correlation between structural distortion and coupling strength. This result also supports the inference that the weakening of the electron-phonon coupling contributes to the blue shift in the emission peak and the narrowing of the FWHM. The reduction in electron-phonon coupling can be attributed to the larger

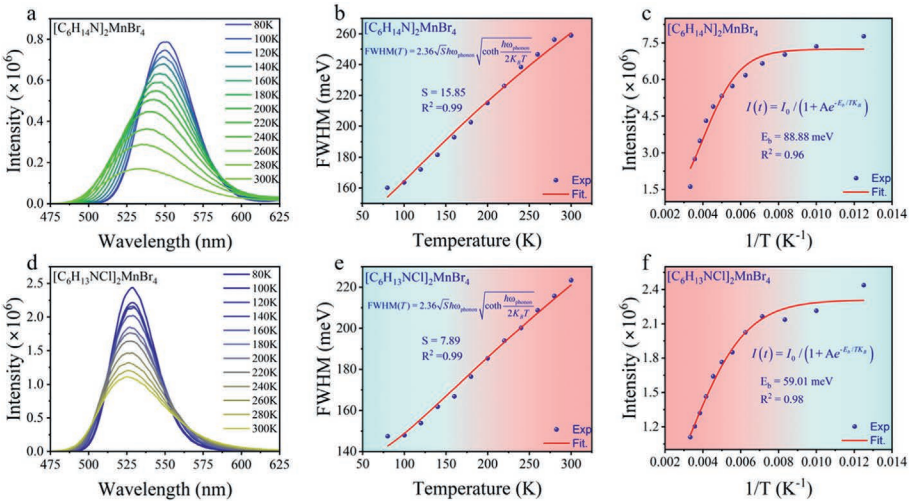



**Fig. 3.** (a) Temperature-dependent PL spectra of $[C_6H_{14}N]_2MnBr_4$. (b) FWHMs of $[C_6H_{14}N]_2MnBr_4$ as a function of temperature under heating conditions. (c) PL intensities of $[C_6H_{14}N]_2MnBr_4$ as a function of $1/T$ under heating conditions. (d) Temperature-dependent PL spectra of $[C_6H_{13}NCl]_2MnBr_4$. (e) FWHMs of $[C_6H_{13}NCl]_2MnBr_4$ as a function of temperature under heating conditions. (f) PL intensities of $[C_6H_{13}NCl]_2MnBr_4$ as a function of $1/T$ under heating conditions.

space occupied by $[C_6H_{13}NCl]^+$, which enhances the structure ordering and reduces the distortion of the $[MnBr_4]^{2-}$ tetrahedron, thereby decreasing the interaction between electrons and lattice vibrations [40,41]. The relationship between PL intensity and temperature was further fitted using the Arrhenius equation:

$$I(t) = I_0/\left(1 + Ae^{-E_b/TK_B}\right) \quad (2)$$

where $I(t)$ is the PL intensity at the experimental temperature, $I_0$ is the PL intensity at 0 K, A is a constant, $K_B$ is the Boltzmann constant, $E_b$ is the exciton binding energy. By applying Eq. 2 for fitting, the fitted $E_b$ value of $[C_6H_{14}N]_2MnBr_4$ is 88.88 meV (Fig. 3c), and the fitted $E_b$ value of $[C_6H_{13}NCl]_2MnBr_4$ is 59.01 meV (Fig. 3f). Both of these values are higher than the room temperature thermal energy (~25 meV), indicating that both materials can stably form excitons. A larger $E_b$ value means that excitons do not easily dissociate before radiative recombination, thus increasing the probability of radiative recombination and facilitating efficient luminescence. $[C_6H_{13}NCl]_2MnBr_4$ exhibits a higher quantum yield because, on one hand, the introduction of chlorine atoms increases the Mn-Mn distance, reducing energy dissipation between adjacent tetrahedra. On the other hand, the weaker interaction between electrons and lattice vibrations reduces the non-radiative recombination probability and increases the radiative recombination probability. In contrast, $[C_6H_{14}N]_2MnBr_4$, although having higher exciton stability, has enhanced electron-phonon coupling, which increases the potential non-radiative transition pathways, thus limiting its quantum yield.

To further clarify the PL mechanism, we investigated their electronic structures and energy transition mechanisms. Firstly, we analyzed the band structures of $[C_6H_{14}N]_2MnBr_4$ (Fig. 4a) and $[C_6H_{13}NCl]_2MnBr_4$ (Fig. 4b) adopting the density functional theory (DFT) calculations. For $[C_6H_{14}N]_2MnBr_4$, the valence band maximum (VBM) and the conduction band minimum (CBM) are not located at the same K-point, which indicates that this material has an indirect band gap. This means that phonons are required to participate in the recombination of electrons and holes for luminescence, so its luminous efficiency will be affected to some extent. However, for $[C_6H_{13}NCl]_2MnBr_4$, the VBM and CBM are located at the same K-point, demonstrating an obvious direct band gap characteristic. This implies that when the material absorbs energy, electrons can directly transit from the valence band to the conduction band, making it easier to generate photons.

Furthermore, we can also find that the band gap of $[C_6H_{13}NCl]_2MnBr_4$ (1.86 eV) is smaller than that of $[C_6H_{14}N]_2MnBr_4$ (2.24 eV). This is because the electron-withdrawing atom Cl significantly stabilizes the conduction band energy of the compound. The increase in the band gap caused by lattice expansion is less than the decrease in the band gap caused by the stabilization of the conduction band energy of the compound. The calculated band gaps are all lower than the experimentally obtained ones because standard DFT calculations usually underestimate the band gaps of materials. As shown in Figs. 4d and e, both the VBM and CBM of $[C_6H_{14}N]_2MnBr_4$ and $[C_6H_{13}NCl]_2MnBr_4$ are mainly composed of Mn-d and Br-p orbitals. Therefore, the D-d transition is the main optical transition process in both materials (Fig. 4c).

The environmental and thermal stability of metal halides are critical determinants for their practical implementation in optoelectronic devices. To systematically evaluate these properties, we conducted comprehensive stability assessments on both $[C_6H_{14}N]_2MnBr_4$ and $[C_6H_{13}NCl]_2MnBr_4$ compounds. Thermogravimetric analysis (Fig. S6 in Supporting information) demonstrates distinct thermal stability profiles: $[C_6H_{14}N]_2MnBr_4$ maintains structural stability below 175 °C, while the chlorinated compound $[C_6H_{13}NCl]_2MnBr_4$ exhibits enhanced thermal resistance, showing negligible decomposition up to 212 °C. Complementary environmental stability tests under ambient conditions (30 %–60 % RH and 10–23 °C) further highlight improvement of stability. As shown in Figs. 5a and d, $[C_6H_{14}N]_2MnBr_4$ suffers severe moisture-induced degradation after four months' air exposure, whereas $[C_6H_{13}NCl]_2MnBr_4$ retains its morphological integrity. This observation is corroborated by XRD analysis (Fig. S7 in Supporting information), where the chlorinated compound $[C_6H_{13}NCl]_2MnBr_4$ maintains phase purity comparable to its pristine state, confirming superior crystallinity stability. The substantial improvement in both thermal and environmental stability through chlorine incorporation. Chlorinated cations establish stronger intermolecular interactions with the $[MnBr_4]^{2-}$ framework, effectively stabilizing the crystal lattice against thermal decomposition. Furthermore, the enlarged molecular volume and enhanced hydrophobicity of chlorinated cations create a protective surface barrier. This dual mechanism physically isolates the $[MnBr_4]^{2-}$ centers from environmental reactants (*e.g.*, $H_2O$, $O_2$), thereby suppressing oxidation and hydrolysis pathways. Such structural engineering provides a generalizable strategy for developing stable metal halides.

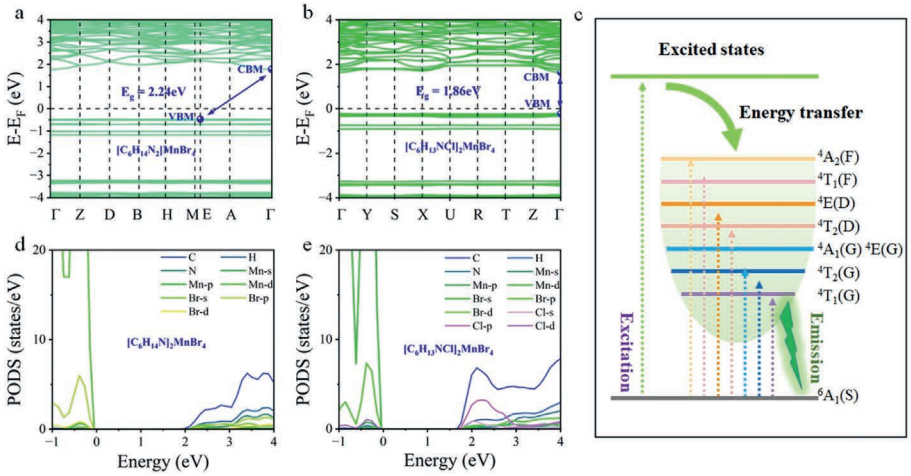



**Fig. 4.** (a) Electronic band structure of $[C_6H_{14}N]_2MnBr_4$. (b) Electronic band structure of $[C_6H_{13}NCl]_2MnBr_4$. (c) Schematic diagram of the energy transfer process of $[C_6H_{14}N]_2MnBr_4$ and $[C_6H_{13}NCl]_2MnBr_4$. (d) Density of states of $[C_6H_{14}N]_2MnBr_4$. (e) Density of states of $[C_6H_{13}NCl]_2MnBr_4$.

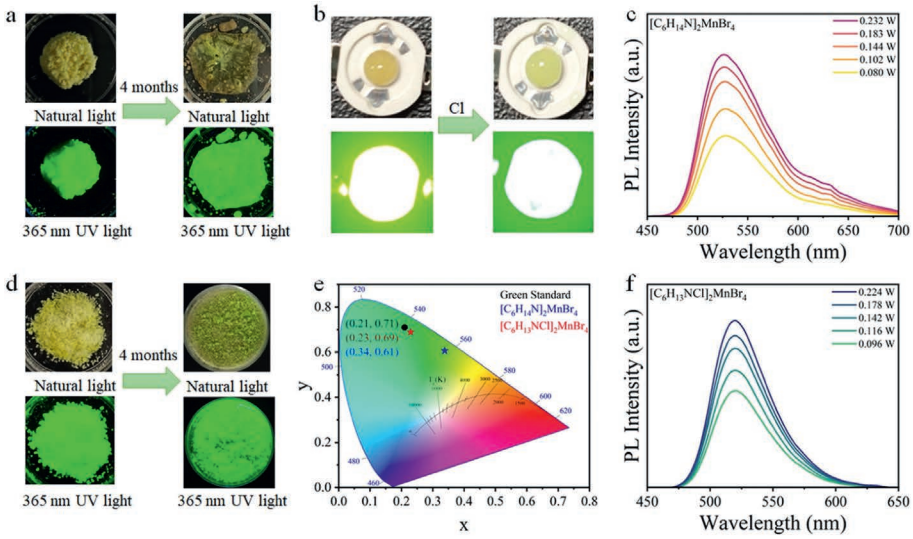



**Fig. 5.** (a) Photos of fresh $[C_6H_{14}N]_2MnBr_4$ powder (left) and photos of $[C_6H_{14}N]_2MnBr_4$ powder (right) after being exposed to air for four months. (b) Photos of the devices based on $[C_6H_{14}N]_2MnBr_4$ (left) and $[C_6H_{13}NCl]_2MnBr_4$ (right). (c) PL spectra of LED based on $[C_6H_{14}N]_2MnBr_4$ driven at different powers. (d) Photos of fresh $[C_6H_{13}NCl]_2MnBr_4$ powder (left) and photos of $[C_6H_{13}NCl]_2MnBr_4$ powder (right) after being exposed to air for four months. (e) CIE coordinates of LED based on $[C_6H_{14}N]_2MnBr_4$ (blue star), $[C_6H_{13}NCl]_2MnBr_4$ (red star) and green standard (black circle). (f) PL spectra of LED based on $[C_6H_{14}N]_2MnBr_4$ were driven at different powers.

Building upon these stability enhancements, we fabricated light-emitting diodes (LEDs) to evaluate the materials' optoelectronic potential. Fig. 5b presents comparative images of operational devices under ambient and driven (3.2 V) conditions. Chromaticity analysis reveals a significant spectral shift upon chlorine substitution: The CIE coordinates transition from (0.34, 0.61) for $[C_6H_{14}N]_2MnBr_4$ to (0.23, 0.69) for the chlorinated compound (Fig. 5e), approaching the standard green emission (0.21, 0.71) specified in the CIE 1931 chromaticity diagram. Notably, both materials exhibit excellent color stability under varying drive powers (Figs. 5c and f), with emission intensities showing linear correlation to input power (a critical characteristic for high-brightness applications). The corresponding fitting plots are shown in Fig. S8 (Supporting information). The combination of enhanced environmental resilience and stable electroluminescent performance positions these Mn-based OIMHs as promising candidates for solid-state lighting technologies.

Moreover, to investigate the molecular mechanisms underlying the luminescence enhancement and stability of the chlorinated compound, we conducted a systematic Hirshfeld surface analysis on their organic cations. Both materials share identical $[MnBr_4]^{2-}$ tetrahedron, enabling focused comparison of cation-driven interactions. Fig. 6 displays surfaces color-mapped by intermolecular distances: red (less than van der Waals radii sum), white (near van der Waals radii sum), and blue (greater than van der Waals radii sum). In the $[C_6H_{14}N]^+$ system, the H···H contact dominates the intermolecular interactions with a contribution of 63.4 %, far exceeding the H···Br (36.5 %) and other weak interactions (H···Mn only 0.1 %) (Fig. 6a). This high proportion of H···H contacts significantly enhances the Coulombic repulsion between the cations, leading to a more loosely packed lattice structure.

After introducing the chlorine atom, the H···H contact ratio in $[C_6H_{13}NCl]^+$ decreases to 42.7 %, while a new H···Cl interaction appears, contributing 21.9 %. This reorganization of interactions creates a more balanced attractive-repulsive network: H···Br (32.2 %) and H···Cl cooperatively enhance the cation-$[MnBr_4]^{2-}$ host-guest attraction, while the optimized H···H ratio (42.7 % *vs.* 63.4 %) effectively alleviates the cation repulsion (Fig. 6b). X-ray refinement analyses reveal that chlorination substantially reduces the Mn–Br bond length deviation from 0.069 Å to 0.012 Å (Fig. S5). The spe-

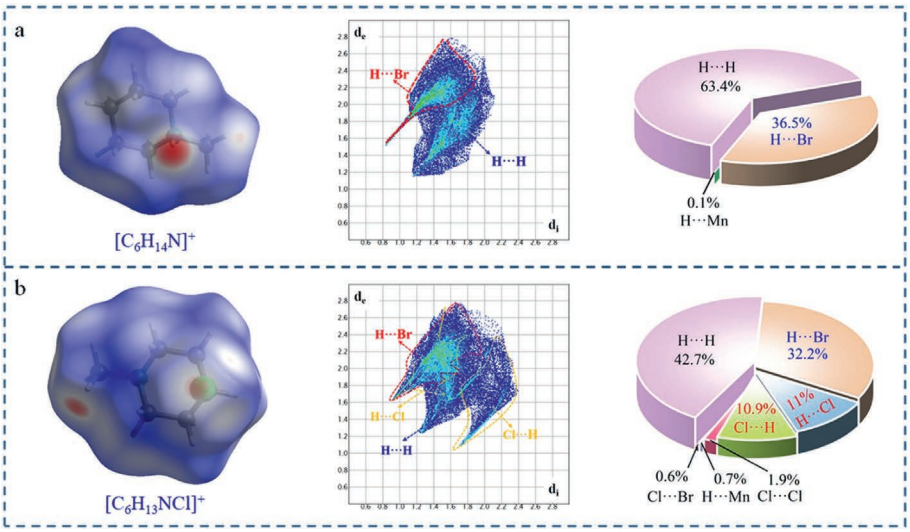



**Fig. 6.** Hirshfeld surface and fingerprint plots for (a) $[C_6H_{14}N]^+$ in $[C_6H_{14}N]_2MnBr_4$, (b) $[C_6H_{13}NCl]^+$ in $[C_6H_{13}NCl]_2MnBr_4$.

cific bond lengths are shown in Tables S2 and S3 (Supporting information). This structural optimization arises from the strong electronegativity of Cl (Pauling $\chi = 3.14$) [42], which enhances electrostatic coupling between organic cations and the $[MnBr_4]^{2-}$ framework *via* electronic polarization effects, thereby suppressing Jahn-Teller distortions in the Br coordination environment. This suppressed Jahn-Teller distortion correlates with tighter molecular packing and uniform force distribution, fostering robust hydrogen bonding and van der Waals networks. The resultant defect-minimized crystalline architecture directly accounts for the observed enhancements in both environmental stability and fluorescence quantum yield.

In summary, we have successfully designed two 0D Mn-based OIMHs ($[C_6H_{14}N]_2MnBr_4$ and $[C_6H_{13}NCl]_2MnBr_4$) and effectively improved the luminescence performance and stability of $[C_6H_{13}NCl]_2MnBr_4$ through the chlorination effect. Both of them exhibit green light emission under 363 nm excitation, which is attributed to the d-d transition ($^4T_1 - ^6A_1$) of the tetrahedral coordinated $Mn^{2+}$ center. The presence of the Cl atom leads to an increase in the occupied space of $[C_6H_{13}NCl]^+$, thereby suppressing excitation energy transfer between adjacent $Mn^{2+}$ centers, resulting in an approximately one-fold increase in PLQY (from 38.8 % to 74.5 %). Additionally, $[C_6H_{13}NCl]_2MnBr_4$ demonstrates superior environmental stability due to the increased H···Cl interactions. Moreover, $[C_6H_{13}NCl]_2MnBr_4$ possesses CIE color coordinates (0.23, 0.69) closer to the NTSC green standard compare to $[C_6H_{14}N]_2MnBr_4$. Our work not only provides new insights into the relationship between the structure and optical properties of manganese-based metal halides but also offers a promising material for next-generation optoelectronic applications.

## Accession codes

CCDC 2444704–2444705 contain the supplementary crystallographic data for this paper. These data can be obtained free of charge via www.ccdc.cam.ac.uk/data_request/cif, or by emailing data_request@ccdc.cam.ac.uk, or by contacting The Cambridge Crystallographic Data Centre, 12 Union Road, Cambridge CB2 1EZ, UK; fax: +44 1223 336033.

## CRediT authorship contribution statement

**Xiulian Cai:** Writing – original draft, Methodology, Data curation. **Qilin Wei:** Software. **Yaping Gong:** Software. **Tong Chang:** Writing – review & editing, Methodology, Funding acquisition, Conceptualization. **Tongtong Kou:** Methodology. **Ziyang Song:** Validation. **Zengshan Yue:** Data curation. **Huanxin Su:** Methodology. **Yuanxiang You:** Investigation. **Chengmin Ji:** Conceptualization. **Xinxin Han:** Software. **Shiguo Han:** Writing – review & editing, Funding acquisition. **William W. Yu:** Writing – review & editing, Project administration, Funding acquisition, Conceptualization.

## Declaration of competing interest

The authors declare that they have no known competing financial interests or personal relationships that could have appeared to influence the work reported in this paper.

## Acknowledgments

This work was supported by the National Natural Science Foundation of China (Nos. 22205233, 62405165, 62374104), Taishan Scholar Foundation of Shandong Province (No. tsqn202408058), Basic and Applied Basic Research Foundation of Guangdong Province (No. 2025A1515012289), the Natural Science Foundation of Fuzhou City (No. 2024-Y-020), China Postdoctoral Science Foundation (No. 2024M751789), Postdoctoral Innovative Projects of Shandong Province (No. 202400321), and the Shandong Provincial Natural Science Foundation (No. ZR2024QB208).

## Supplementary materials

Supplementary material associated with this article can be found, in the online version, at doi:10.1016/j.cclet.2025.111515.

## References

[1] Q. Tan, Z. Li, G. Luo, et al., Nature 620 (2023) 545–551.
[2] H. Cho, S.H. Jeong, M.H. Park, et al., Science 350 (2015) 1222–1225.
[3] Q. Liao, X. Jin, H. Fu, Adv. Opt. Mater. 7 (2019) 1900099.
[4] H. Lian, Y. Li, S. Saravanakumar, et al., Coord. Chem. Rev. 452 (2022) 214313.
[5] Z. Luo, Y. Liu, Y. Liu, et al., Adv. Mater. 34 (2022) 2200607.
[6] L.J. Xu, X. Lin, Q. He, et al., Nat. Commun. 11 (2020) 4329.
[7] S. Han, G.E. Wang, G. Xu, J. Luo, Z. Sun, Fundam. Res. 3 (2023) 362–368.
[8] L. Yang, X. Liu, B. Li, et al., Chin. Chem. Lett. 37 (2026) 110858.
[9] Z. Li, H. Li, Y. Li, et al., Chin. Chem. Lett. 36 (2025) 109800.
[10] J.T. Mo, Z. Wang, Chin. Chem. Lett. 35 (2024) 109360.
[11] L. Zhou, J.F. Liao, Z.G. Huang, et al., Angew. Chem. Int. Ed. 58 (2019) 15581–15586.
[12] D. Liang, H. Xiao, W. Cai, et al., Adv. Opt. Mater. 11 (2023) 2202997.
[13] W. Ning, F. Gao, Adv. Mater. 31 (2019) 1900326.

[14] Q. Fan, G.V. Biesold-McGee, J. Ma, et al., Angew. Chem. Int. Ed. 59 (2020) 1030–1046.
[15] H. Peng, T. Huang, B. Zou, et al., Nano Energy 87 (2021) 106166.
[16] G.L. Yang, H.Z. Zhong, Chin. Chem. Lett. 27 (2016) 1124–1130.
[17] Y. Zhang, L. Zhou, L. Zhang, et al., Chin. Chem. Lett. 34 (2023) 107556.
[18] Q. Jia, T. Shao, L. Tong, et al., Chin. Chem. Lett. 34 (2023) 107539.
[19] X. Zhu, Y. Zhao, S. Zhang, et al., J. Phys. Chem. C 125 (2021) 27800–27809.
[20] G. Zhou, Z. Liu, J. Huang, et al., J. Phys. Chem. Lett. 11 (2020) 5956–5962.
[21] S. Chen, M. Huang, Y. Yin, J. Shi, Mikrochim. Acta 190 (2023) 329-329.
[22] S. Chen, C. Guo, S.C. Chen, et al., Small 20 (2024) 2406032.
[23] T. Jiang, W. Ma, H. Zhang, et al., Adv. Funct. Mater. 31 (2021) 2009973.
[24] S. Wang, X. Han, T. Kou, et al., J. Mater. Chem. C 9 (2021) 4895–4902.
[25] J.B. Luo, J.H. Wei, Z.Z. Zhang, Z.L. He, D.B. Kuang, Angew. Chem. Int. Ed. 62 (2023) 202216504.
[26] P. Liu, Y. Sun, A.J. Fernández-Carrión, et al., Chin. Chem. Lett. 35 (2024) 108641.
[27] K. Li, W. Zhang, L. Niu, et al., Adv. Sci. 10 (2023) 2204843.
[28] X. Zhao, M. Wu, H. Liu, et al., Adv. Funct. Mater. 32 (2021) 2109277.
[29] G. Zhou, Q. Ren, M.S. Molokeev, et al., ACS Appl. Electron. Mater. 3 (2021) 4144–4150.
[30] H.M. Pan, Q.L. Yang, X.X. Xing, et al., Chem. Commun. 57 (2021) 6907–6910.
[31] Y.L. Wei, J. Jing, C. Shi, et al., Inorg. Chem. Front. 5 (2018) 2615–2619.
[32] L. Zhou, J.F. Liao, D.B. Kuang, Adv. Opt. Mater. 9 (2021) 2100544.
[33] J.B. Luo, J.H. Wei, Z.L. He, et al., Chem. Sci. 15 (2024) 16338–16346.
[34] J. Lin, Z. Guo, N. Sun, et al., Inorg. Chem. 61 (2022) 15266–15272.
[35] T. Chang, Q. Wei, Z. Wang, et al., J. Phys. Chem. Lett. 13 (2022) 3682–3690.
[36] T. Chang, Y. Dai, Q. Wei, et al., ACS Appl. Mater. Interfaces 15 (2023) 5487–5494.
[37] Y. Liu, J. Zhang, B. Han, et al., J. Am. Chem. Soc. 142 (2020) 6649–6660.
[38] T. Kou, Q. Wei, T. Chang, et al., Laser Photonics Rev. 19 (2024) 2400953.
[39] T. Chang, Q. Wei, R. Zeng, et al., J. Phys. Chem. Lett. 12 (2021) 1829–1837.
[40] Y. Gao, Q. Wei, T. Chang, et al., J. Mater. Chem. C 11 (2023) 8486–8494.
[41] T. Chang, L. Wang, T. Kou, et al., Carbon Energy 7 (2025) e70016.
[42] A.M. James, C.J. Laconsay, J.M. Galbraith, J. Phys. Chem. A 121 (2017) 5190–5195.